Fabrication of 3D NiO-YSZ structures for enhanced performance of solid oxide fuel cells and electrolysers

I. Jang [*], G.H. Kelsall

Department of Chemical Engineering, Imperial College London, London SW7 2AZ, UK

ARTICLE INFO

ABSTRACT

Increasing densities of (electrode–electrolyte-pore) triple phase boundaries (TPBs) / reaction sites enhance performances of solid oxide electrochemical reactors (SOERs) in both fuel cell (SOFC) and electrolyser (SOE) modes. Inkjet 3D printing is capable of construction of ceramic microstructures on support layers, enabling fabrication of SOERs with enhanced active area to geometric area ratios, thereby up-scaling effective areas / TBP lengths per unit volume.

A Ni(O)-YSZ functional layer was designed and 3D inkjet printed with a surface of circular pillars, a facile geometry for printing that increased the interfacial to geometric area ratio. Deposition of further functional layers and sintering resulted in fully fabricated reactors with structures: H_2O-H_2 | Ni(O)-YSZ support | Ni(O)-YSZ pillars | YSZ | YSZ-LSM | O_2, Air. The corresponding planar structured cell also was fabricated with the same components, for comparison of its electrochemical performance with that of the pillar-structured cell. The latter exhibited performance enhancement over its planar counterpart by factors of ca. 1.5 in fuel cell mode, ca. 3 in steam electrolysis mode, and ca. 4–5 in CO_2 electrolysis mode, thereby demonstrating the potential of geometric structuring of electrode | electrolyte interfaces by 3D printing for developing higher performance SOERs.

1. Introduction

Increasing consequences of global climate change are increasing demand for environmentally benign gas conversion processes, such as H_2O conversion for clean H_2 fuel production, or CO_2 conversion for achieving carbon neutrality [1–3]. Among the various types of electrochemical gas conversion systems, due to their high conversion efficiencies, SOERs are becoming one of the highest potential gas conversion systems for the future, enabling environmentally benign reduction of CO_2 or H_2O, when powered from renewable energy sources [4–7].

Increasing densities of reaction sites at electrode | electrolyte | pore triple phase boundaries (TPBs), enable decreased potential losses at constant current density, so increasing energy conversion efficiencies [8–11]. Numerous publications have reported using various technologies to fabricate 3D structured electrolyte or electrode layers, effectively increasing TPB densities [12–15]. Among those technologies, 3D inkjet printing is the most effective and practical means of constructing 3D structured component layers [16] and is now available commercially incorporating conveyer belt systems, offering the prospect of mass production of ceramic SOERs [17,18].

Farandos et al. [19] printed YSZ pillar structures by inkjet printing to increase the interfacial area between the electrolyte and air electrode layer and Masciandaro et al. [20] reported validation of its effect on the enhanced electrochemical cell performance. However, such YSZ electrolyte pillar structures have extended ion conduction paths through the pillars, resulting in increasing potential drops and so decreasing local current densities with increasing pillar heights, limiting their optimal values [21]. The greater conductivities of Ni(O)-YSZ pillars would enable extension of their heights, limited by their mechanical strength, so allowing greater extension of surface area and reaction site densities than can be achieved with YSZ pillar structures.

Herein, fabrication by 3D inkjet printing of Ni(O)-YSZ pillar structures is reported to enhance effective reaction areas by increasing interfacial areas between Ni(O)-YSZ electrodes and YSZ electrolyte layers. For validation of the effect, two types of cells were fabricated as shown in Fig. 1: Planar (a) and Pillar (b). We also report the electrochemical performance of the SOERs in both fuel cell and electrolyser modes, in the latter case with both steam and CO_2 electrolysis. In a subsequent publication, predicted and experimentally validated effects

* Corresponding author.
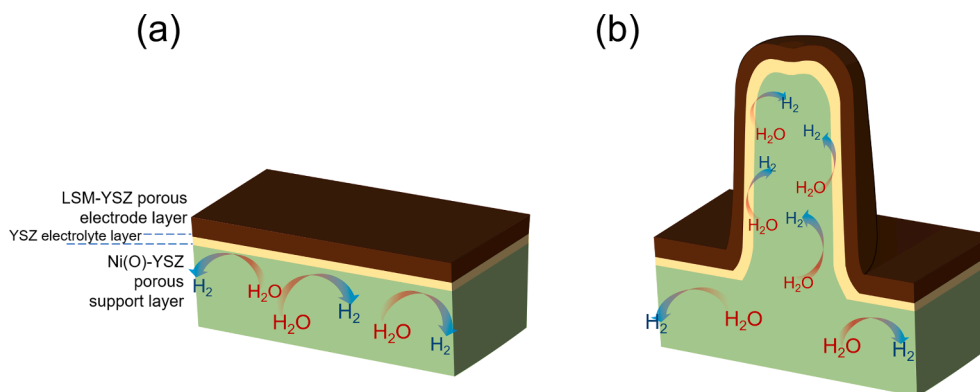*E-mail address:* i.jang@imperial.ac.uk (I. Jang).

Fig. 1. Schematic illustration of (a) planar and (b) pillar structured solid oxide electrochemical reactors, represented in steam electrolysis mode.

of pillar heights and diameters on the electrochemical properties of SOERs will be addressed.

2. Experimental

2.1. Ink-preparation & printing

NiO-YSZ inks were formulated for printing by mixing NiO powder (NiO-F, FuelCellMaterials, USA) and YSZ powder (YSZ8-U1, FuelCell-Materials, USA) in a 1 to 1 wt ratio and dispersed in water of neutral pH. Dispex A40 (Ciba-BASF, UK) was added at dispersant concentrations corresponding to 0.2 mg m^{-2} of the powder's specific surface area, and the powder was ball milled at 70 rpm for 48 h. The subsequent YSZ ink formulation was as published previously [19] with minor adjustments. The ball-milled ink was sonicated using a rod-shaped ultrasonic probe (Q55, QSonica, USA) for 3 min and repeated twice with 3 min intervals. The ink was then subjected to further sonication in an ultrasonic bath (SQ-US-1025, Sciquip, UK) for 10 min, and then centrifuged at 1400 rpm for 2 min, followed by 1000 rpm for 5 min. PEG 35,000 was added with a 25 mg cm^{-3} ratio of the ink volume, and stirred for 24 h. Natsurf 265 (Croda Chemicals, UK) was added at a concentration of 0.2 mg cm^{-3}, just before printing. The ejection pulse rate for the printing was 4 kHz, corresponding to a 74.6 mm s^{-1} printing speed; pillars were printed with 50 μm diameter and 100 μm inter-pillar (centre) spacing.

Experimental explanation for anode support layer preparation and microstructural characterisation is described in supplementary information.

2.2. Electrochemical analysis

Electrochemical kinetic measurements were made in both fuel cell and electrolysis modes. Silver paste was applied to the LSM-YSZ electrode layer and silver mesh (silver gauze, Alfa Aesar, USA) was attached as a current collector; 0.4 mm diameter and Pt wire was used to connect both electrodes to the potentiostat. The cell was attached to one end of a 25 mm outer diameter alumina tube and sealed with a ceramic sealant (Adhesive 668, Aremco, USA).

Mass flow controllers (F-201CV, Bronkhorst, Netherlands) were used to control flow rates of hydrogen/water vapour/CO_2/CO gas on the Ni (O)-YSZ support layer and air to the positive electrode. A vapour flow controller (CEM W-101A, Bronkhorst, Netherland) was used to control water vapour flow rates, diluted with Ar carrier gas, the flow rate of which was also controlled by mass flow controller. The cell was placed in a vertical tube furnace (TS1 12/60/300, Carbolite-Gero, UK) to maintain its temperature.

The attached cell was first heat-treated at 200 °C to cure the ceramic adhesive paste and then increased to 700 °C at 5 °C min^{-1}. Then the Ni (O) negative electrode was reduced with 10 % hydrogen in Ar carrier gas, for 18 h at 700 °C. Subsequently, electrochemical measurements were made at 700 °C, 750 °C, and 800 °C.

A potentiostat (PGSTAT302N, Ecochemie, Metrohm, The Netherlands) was used to measure current–potential difference data and
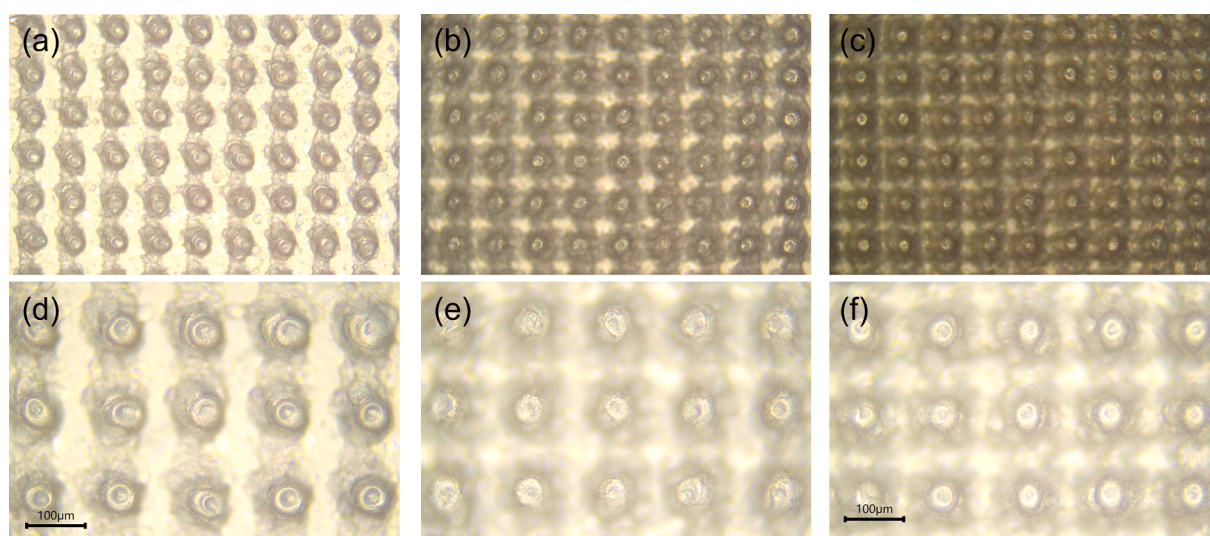

Fig. 2. Optical microscope images of as-printed Ni(O)-YSZ arrays with: (a) 30 layers, (b) 60 layers and (c) 90 layers of printings, with 50 μm diameter and 100 μm spacing. Higher magnification images of (d) 30 layers, (e) 60 layers and (f) 90 layers printed pillars.
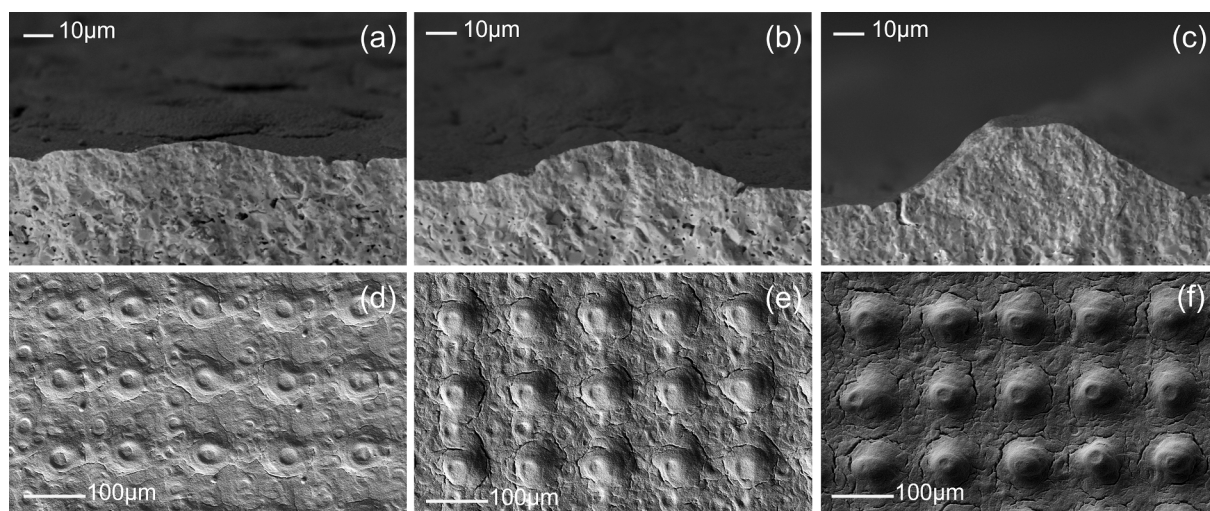
Fig. 3. SEM images of Ni(O)-YSZ pillar structures after sintering at 1450 °C for 5 h, with cross view of (a) 30 layers, (b) 60 layers and (c) 90 layers of printing, and top view of (d) 30 layers, (e) 60 layers and (f) 90 layers printed pillars.

impedance spectra of the cell at each of the three working temperatures. Impedance measurements were made in the frequency range of 10^5–0.1 Hz under open circuit potential difference conditions. Current density-potential difference data were determined at a potential sweep rate of 20 mV s^{-1} in both fuel cell and electrolysis modes.

3. Results and discussion

3.1. Printing results & ink property effects on NiO-YSZ ink printing

Optical microscope images in Fig. 2 show the as-printed Ni(O)-YSZ pillar arrays with (a) 30 layers, (b) 60 layers and (c) 90 layers of printings, printed with a 50 μm diameter and 100 μm spacing. From the higher magnification images in Fig. 2d–f, more detailed structures of the pre-sintering Ni(O)-YSZ pillars are evident, composed of organic and inorganic materials prior to sintering. The optical microscopic images enabled non-destructive analysis of the printed deposits prior to expending additional time for sintering. From the images obtained, well-printed pillar structures were evident in as-printed states, together with pillar heights increasing with the number of printed layers. Additionally, from the low magnification image in Fig. S1 in the Supplementary Information, the entire printed pillar array appeared well-constructed and overall, had no missing pillars.

Fig. 3 shows the SEM images of printed pillar structures after sintering at 1450 °C for 5 h. Fig. 3d–f show top view images of the pillar structures, showing crater-like structures arising from the coffee stain effect, due to its viscosity when the ink dried [22]; corresponding cross-sectional images of the pillars are shown in Fig. 3 a-c, from which pillar heights increased with the number of printed layers, as expected; 30 printed layers produced pillars with ca. 10 μm height, 60 layers increased that to 18.7 μm, and 90 layers to ca. 27.8 μm. Those values are slightly less than expected from the optical microscope images, and the cross-sectional pillar image of 90 printed layers in Fig. 3 c appeared a little squat, without the sharp edge evident in as-printed pillar images in Fig. 2. This may have arisen from the low particle concentration (14.78 wt%) in the ink decreasing its desired viscosity. Some large size particles or particle agglomerates in the ink may have been removed in the last filtration step of ink formulation, leading to higher organic material concentrations, causing larger volume losses / changes during the firing / sintering processes. Hence, it would be difficult for pillars to sustain their geometries during sintering at high temperatures, so explaining why printed and sintered pillar geometries depend on particle concentrations in the ink.

When pillars were printed with ink concentrations > 18 wt%, the ratio of organic material in the ink decreased compared to inks with lower particle concentrations, pillars could better sustain their as-printed geometries, as shown in Fig. S2 in the Supplementary Information.

In addition, printer nozzle blockage during printing affects printed pillar properties. Fig. S3 shows a pillar printed from an ink with a particle concentration of ca. 15.9 wt% and lower purging pressure of ca. 200–300 mPa every 10 layers of printing. The first 30 printed layers in Fig. S3a-b, exhibited the printing results with clear pillar structures. However, since the NiO particles used for the printing had a relatively large ca. 450 nm particle size, with repeated printed layers, the particles would have caused nozzle blockages more easily, so that printing properties of the ink degrade, leading to more variability in pillar geometries. To avoid the nozzle blockage during the printing, the pillars shown in Fig. 2 were printed with a higher purging pressure of 500 mPa. The shrinkage ratio of fabricated pillars and its explanation are in the supplementary information file. (Figs. S4–S5, Tables S1–S2).

From Fig. 4, cross-sectional images of squat Ni(O)-YSZ pillar structures covered with YSZ electrolyte layers are shown in (b, d, f), which can be compared with Ni(O)-YSZ structures without YSZ layers in Fig. 4 (a, c, e). The dense YSZ layer coated by dip-coating had a thickness of about 7 μm, indicated with green colour lines, as shown in Fig. 4b. From the image in Fig. 4d, the outer surface of the Ni(O)-YSZ structure appeared to be fully covered with a dense YSZ electrolyte layer without surface defects. Fig. 4e, f show arrays of Ni(O)-YSZ pillars, respectively without and with YSZ layers; the top view of YSZ electrolyte covered Ni (O)-YSZ pillar structures are shown in Fig. S6.

The cross-sectional image of Ni(O)-YSZ pillars in Fig. S5 shows half-cut pillars that are different from those of the Ni(O)-YSZ pillar array covered with YSZ electrolyte layer, shown in Fig. 4f, due to the different location of sample cutline.

3.2. Solid oxide fuel cell (SOFC) performance

Fig. 5 shows the effect of current density on potential differences and power densities for the SOFC fabricated by coating the Ni(O)-YSZ pillars with a YSZ electrolyte layer, as shown in Fig. S8, followed by the YSZ-LSM layer as a positive (air) electrode. Comparison of the current–potential difference-power density data in Fig. 5 for the cells with planar and Ni-YSZ pillars in fuel cell mode, shows that the pillars produced an increase in peak power densities of 30–50 %, respectively, from 33.6, 63.61 and 116 mW cm^{-2} to 54.45, 92.76 and 145.3 mW cm^{-2} at 700 °C, 750 °C and 800 °C, respectively, corresponding to increases of 62, 46 and 25 %, respectively. For determination of the fuel cell
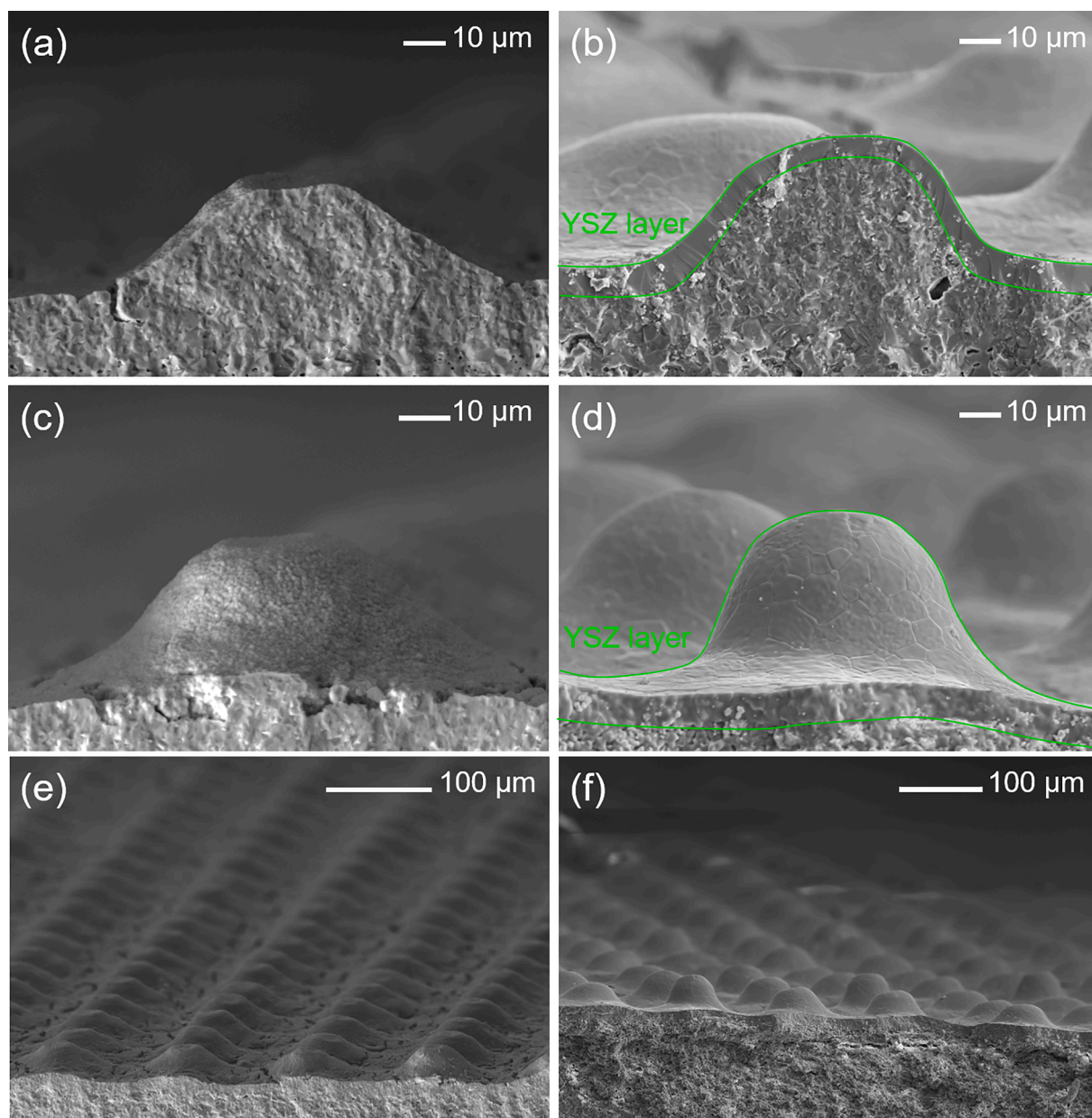
Fig. 4. SEM images of Ni(O)-YSZ pillars without YSZ electrolyte layer (a, c, e) and with YSZ electrolyte layer (b, d, f). Ni(O)-YSZ pillar cross section (a, b), the entire shape of Ni(O)-YSZ pillar without cutting (c, d), and entire array of Ni(O)-YSZ pillars (e, f). The dip-coated YSZ layers in (b) & (d) are indicated with green lines.

performance, air was injected to the positive electrode and H_2 with 3% H_2O gas was injected to the negative electrode.

From the EIS data shown in Fig. 5(c)-(d), the cell with Ni(O)-YSZ pillars exhibited a lower ohmic resistance (R_{ohm}) and polarization resistance (R_p) values, listed in Table S3, at each working temperature. The decrease in both R_{ohm} and R_p derived for the pillar-structured cell, resulted from the increase in both electrolyte | electrode interfacial areas and the number of reaction sites, thereby increasing cell performance [23]. As shown in the Bode plot in Fig. S7, $-Z_{im}$ values decreased in the middle and high frequency range, due to increased electrode areas enhancing reaction site numbers for both oxygen reduction reaction at cathode side and hydrogen oxidation reaction at anode side, thereby promoting charge transfer and surface exchange rates in the electrodes. Low frequency (0.1–1 Hz) values were unaffected, as measurements at open circuit potentials, so neither cell would have been subject to transport limitations [7,24].

Those cells exhibited lower than state-of-the-art power densities

possibly due to its thin LSM-YSZ ca. 4 μm electrode layer (Fig. S8), giving fewer reaction sites in the oxygen electrode layer, resulting in large values of R_p in both cells; the objective was to be able to compare performances of cells with planar and pillared Ni-YSZ, rather than maximising performance. The cells' low performance could be additionally explained by the high potential loss in some part of Pt wire used for a current collector, as the estimated potential drop was ca. 30–50 mV, at the current (ca. 0.4 A) corresponding to the peak power density of planar cell at 800 °C operation temperature.

3.3. Electrolysis performance

3.3.1. H_2O electrolysis performance

Fig. 6 shows the effect of current density on potential difference for both cells operated in H_2O electrolysis mode, by injecting water vapour at the negative electrode. As for fuel cell mode, the electrolysis cell with Ni-YSZ pillared structure exhibited enhanced performance compared to
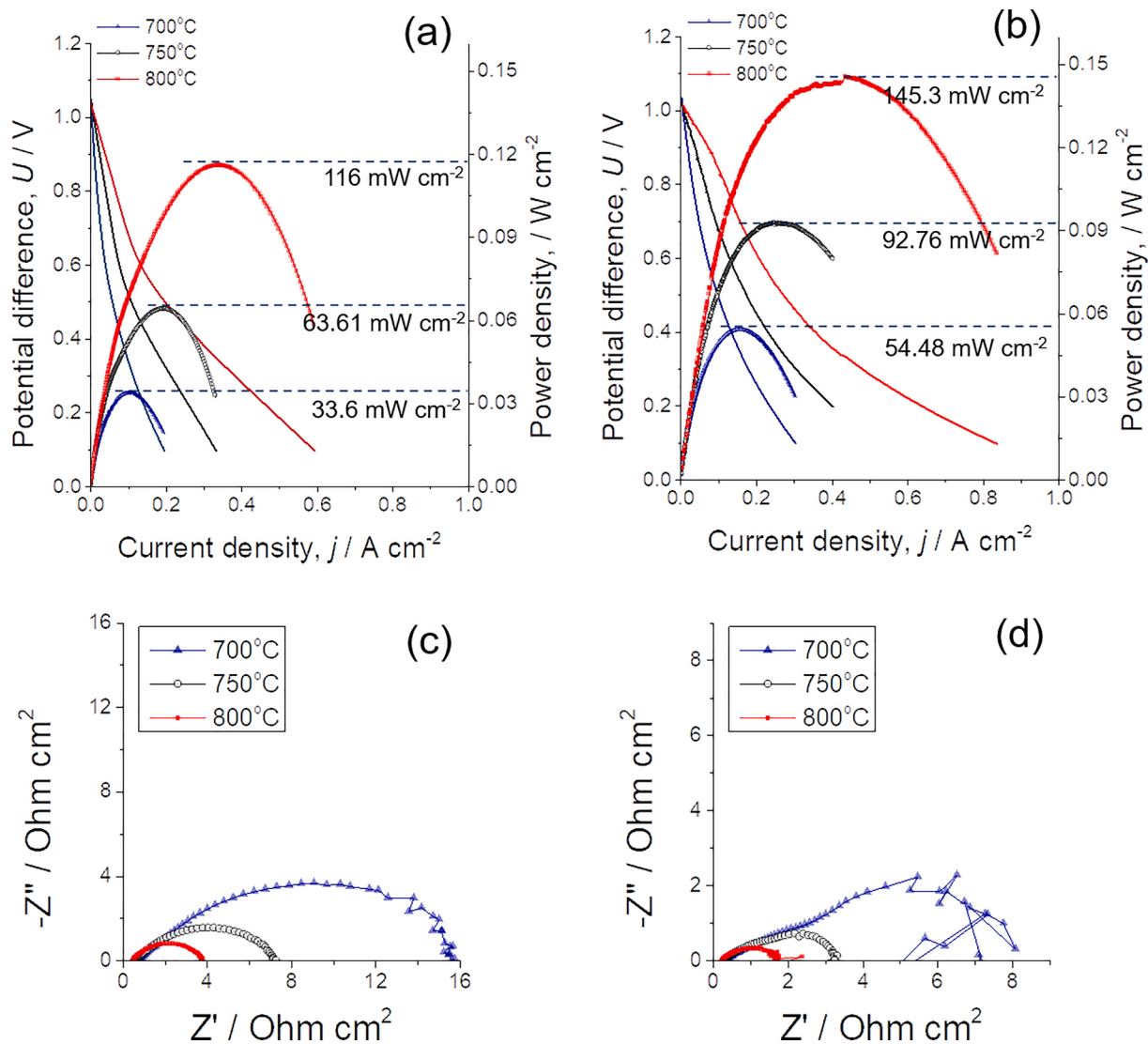
Fig. 5. Effect of current density on potential differences and power densities for: (a) planar cell and (b) Ni(O)-YSZ pillar structured cell operated in fuel cell mode at 700 °C, 750 °C and 800 °C. Electrode impedance spectra for (c) planar cell and (d) Ni(O)-YSZ pillar structured cell measured at open circuit at the same operating temperatures.
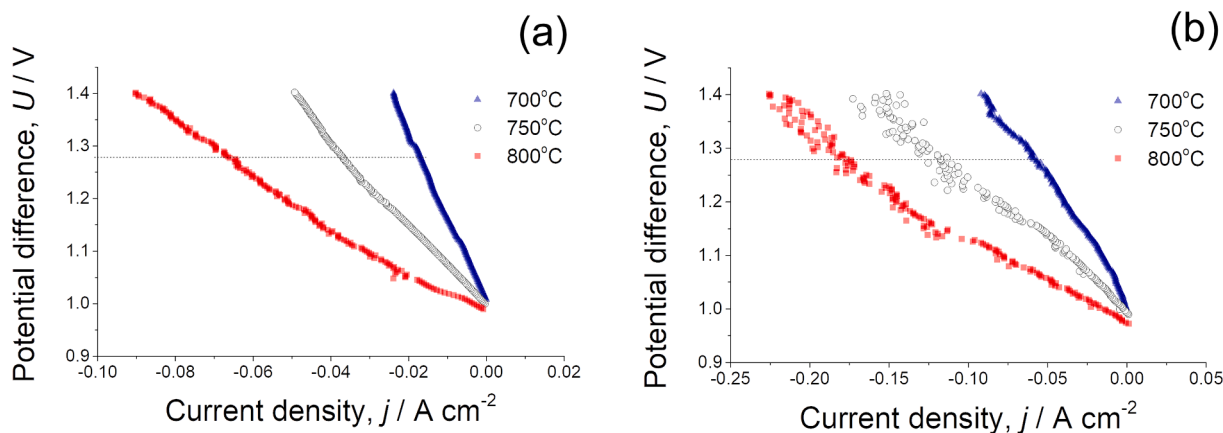

Fig. 6. Effect of current density on potential difference for cells with: (a) planar structure, and (b) Ni(O)-YSZ pillar structure, operated in steam electrolysis mode with wet H_2 (10 % H_2O) / Ar at 700 °C, 750 °C and 800 °C.
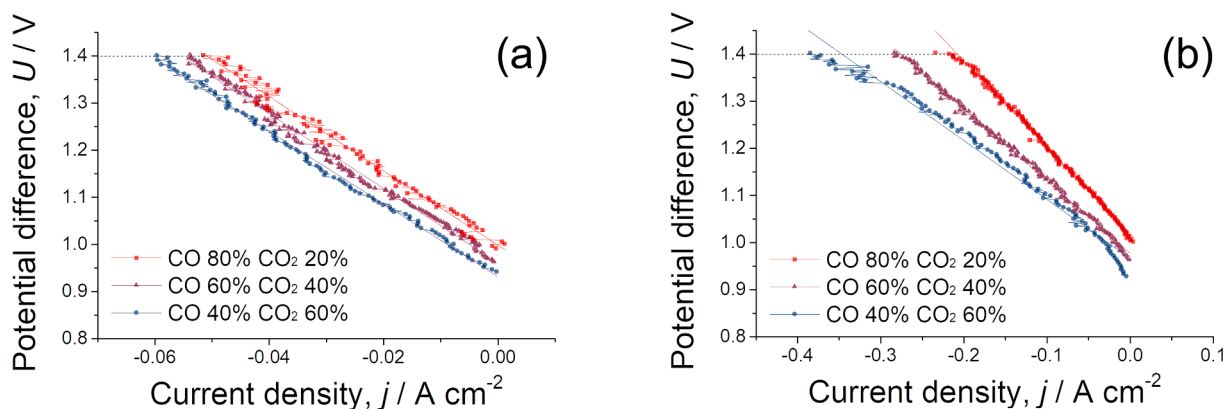
Fig. 7. Effect of current density on potential differences for cells with: (a) planar structure, and (b) Ni(O)-YSZ pillar structure operated in CO_2 electrolysis mode at 750 °C and with various CO/CO_2 gas ratios.

the planar cell increased At the thermoneutral potential difference of ca. 1.28 V [5,25,26], current densities were 0.016 A cm^{-2}, 0.035 A cm^{-2}, and 0.064 A cm^{-2} at 700 °C, 750 °C, and 800 °C, respectively, for the planar cell, and 0.053 A cm^{-2}, 0.111 A cm^{-2} and 0.172 A cm^{-2} for the pillared cell, corresponding to a threefold increase in performance, significantly greater than in fuel cell mode.

The electrolyser with pillared structure showed less stable performance than the planar structured cell with slight current fluctuations at constant potential difference. Minor electrolyte leakage at higher current densities may have resulted from the Ni(O)-YSZ pillar structure being less homogeneously dip-coated by YSZ electrolyte than on the planar structure. However, since the operating potential difference range was ≤ 1.5 V [27], current fluctuations were more possibly caused by the accumulation of water in the exhaust pipeline, as has been reported previously [28].

3.3.2. CO_2 electrolysis performance

Fig. 7 shows the effects of current density on potential differences for CO_2 electrolysis at 750 °C in both cells, with varying CO / CO_2 gas ratios from 80 % to 20 % to 40 % to 60 %. As for steam electrolysis, the cell with a pillar structure exhibited enhanced performance compared to its planar counterpart at a maximum potential difference of 1.4 V, slightly less than the 1.465 V thermoneutral potential for CO_2 electrolysis [29]. At a potential difference of 1.4 V current densities were 0.051 A cm^{-2}, 0.055 A cm^{-2}, and 0.060 A cm^{-2} at (CO 80% CO_2 20%), (CO 40 % CO_2 60 %), and (CO 40 % CO_2 60 %) gas ratios, respectively in the planar cell, compared with 0.208 A cm^{-2}, 0.276 A cm^{-2} and 0.347 A cm^{-2} in the cell with pillared geometry, which exhibited an increased performance by a factor of ca. 4–5. Hence, 3D printing could be a promising technology for the development and production of future high-performance CO_2 conversion systems.

As shown in Figs. 5 to 7, the relative increase of current in the pillared cell relative to the planar structure was greatest for CO_2 electrolysis, slightly less for H_2O electrolysis, and was smallest in H_2 fuel cell mode. Differences in current up-scaling were due to differences in kinetic parameters for the different reactions, including their responses to different gas partial pressures, especially at the Ni-YSZ electrode [30,31]. CO_2 reduction, being slower than H_2O reduction, is more sensitive to increases of TPBs, thereby exhibiting the greatest increase in current at constant potential difference for CO_2 electrolysis in pillared cells. Furthermore, for fuel cell and electrolyser modes, asymmetric kinetic parameters for reduction and oxidation pairs, complicate explanations of differences in current up-scaling of pillared structures in the two modes [32–34]. Additional effects of spatial distributions of potential and current in pillared structures, both model predictions and experimental validation, is the subject of a future report [21].

4. Conclusions

Ni(O)-YSZ functional layers with circular pillar structures were designed and fabricated by inkjet printing, aiming to increase densities of triple phase boundaries per unit geometric area, hence increasing fuel cell and electrolyser performances. Experimental determination of those performances demonstrated enhancement, in electrolyser mode by a factor of ca. 3 for H_2O electrolysis and 4–5 for CO_2 electrolysis. In fuel cell mode, the enhancement factor was a more modest ca. 1.4–1.5 for the range of conditions investigated. Nonetheless, those enhancement factors demonstrate the encouraging prospects of 3D ink-jet printing for the development of more energy efficient and/or compact SOERs, potentially with decreased specific costs. However, optimisation of pillar printing conditions is still needed to optimise Ni(O)-YSZ pillar geometries after sintering, to control pillar height and diameter with sharp pillar edges.

Future publications will address the fabrication of Ni(O)-YSZ pillar structures with various heights and diameters to better define relationships between electrode | electrolyte interfacial geometries, areas and electrochemical performances.

CRediT authorship contribution statement

I. Jang: Conceptualization, Validation, Investigation, Writing – original draft. **G.H. Kelsall:** Writing – review & editing, Supervision, Resources, Project administration, Funding acquisition.

Declaration of Competing Interest

The authors declare the following financial interests/personal relationships which may be considered as potential competing interests: Inyoung Jang, Geoff H Kelsall reports financial support was provided by Shell Global Solutions International BV.

Appendix A. Supplementary data

Supplementary data to this article can be found online at https://doi.org/10.1016/j.elecom.2022.107260.

References

[1] T.A. Schmauss, S.A. Barnett, ACS Energy Lett. 6 (2021) 3180–3184.

[2] S. Perry, J. Klemeś, I. Bulatov, Energy 33 (2008) 1489–1497.
[3] M.H. Barecka, J.W. Ager, A.A. Lapkin, Iscience 24 (2021), 102514.
[4] Y. Song, X. Zhang, K. Xie, G. Wang, X. Bao, Adv. Mater. 31 (2019) 1902033.
[5] J.B. Hansen, Faraday Discuss. 182 (2015) 9–48.
[6] A. Hauch, R. Küngas, P. Blennow, A.B. Hansen, J.B. Hansen, B.V. Mathiesen, M. B. Mogensen, Science 370 (6513) (2020) eaba6118, https://doi.org/10.1126/science.aba6118.
[7] R. Küngas, J. Electrochem. Soc. 167 (2020), 044508.
[8] J.R. Wilson, W. Kobsiriphat, R. Mendoza, H.-Y. Chen, J.M. Hiller, D.J. Miller, K. Thornton, P.W. Voorhees, S.B. Adler, S.A. Barnett, Nat. Mater. 5 (2006) 541–544.
[9] Y.B. Kim, C.-M. Hsu, S.T. Connor, T.M. Gür, Y. Cui, F.B. Prinz, J. Electrochem. Soc. 157 (2010) B1269.
[10] P.A. Connor, X. Yue, C.D. Savaniu, R. Price, G. Triantafyllou, M. Cassidy, G. Kerherve, D.J. Payne, R.C. Maher, L.F. Cohen, Adv. Energy Mater. 8 (2018) 1800120.
[11] J.M. Vohs, R.J. Gorte, Adv. Mater. 21 (2009) 943–956.
[12] I. Jang, S. Kim, C. Kim, H. Yoon, T. Song, J. Power Sour. 392 (2018) 123–128.
[13] J. An, Y.-B. Kim, J. Park, T.M. Gür, F.B. Prinz, Nano Lett. 13 (2013) 4551–4555.
[14] A. Pesce, A. Hornés, M. Núñez, A. Morata, M. Torrell, A. Tarancón, J. Mater. Chem. A 8 (2020) 16926–16932.
[15] K. Miyamoto, H. Koga, M. Izumi, M. Mizui, H. Nishiguchi, ECS Trans. 96 (2020) 219.
[16] J. Ruiz-Morales, A. Tarancón, J. Canales-Vázquez, J. Méndez-Ramos, L. Hernández-Afonso, P. Acosta-Mora, J.M. Rueda, R. Fernández-González, Energy Environ. Sci. 10 (2017) 846–859.
[17] M. Lira, N. Kostretsova, S. Anelli, A. Morata, M. Torrell, A. Tarancón, in: ECS Meeting Abstracts, IOP Publishing, 2021, MA2021-03, 14. https://doi.org/10.1149/MA2021-03114mtgabs.
[18] V. Esposito, C. Gadea, J. Hjelm, D. Marani, Q. Hu, K. Agersted, S. Ramousse, S. H. Jensen, J. Power Sources 273 (2015) 89–95.
[19] N. Farandos, L. Kleiminger, T. Li, A. Hankin, G.H. Kelsall, Electrochim. Acta 213 (2016) 324–331.
[20] S. Masciandaro, M. Torrell, P. Leone, A. Tarancón, J. Eur. Ceram. Soc. 39 (2019) 9–16.
[21] I. Jang, J.C. Alexander, N.M. Farandos, G.H. Kelsall, Predicting Optimal Geometries of 3D-Printed Solid Oxide Electrochemical Reactors, Electrochim. Acta, Submitted (2022).
[22] A. Friederich, J.R. Binder, W. Bauer, J. Am. Ceram. Soc. 96 (2013) 2093–2099.
[23] H. Moon, S.D. Kim, E.W. Park, S.H. Hyun, H.S. Kim, Int. J. Hydrogen Energy 33 (2008) 2826–2833.
[24] M.-B. Choi, H. Shin, H.-I. Ji, H. Kim, J.-W. Son, J.-H. Lee, B.-K. Kim, H.-W. Lee, K. J. Yoon, JOM 71 (2019) 3825–3834.
[25] A. Buttler, H. Spliethoff, Renew Sust Energy Rev 82 (2018) 2440–2454.
[26] L. Kleiminger, T. Li, K. Li, G. Kelsall, Electrochim. Acta 179 (2015) 565–577.
[27] C. Cheng, G. Kelsall, L. Kleiminger, J. Appl. Electrochem. 43 (2013) 1131–1144.
[28] D. Klotz, A. Weber, E. Ivers-Tiffée, Electrochim. Acta 227 (2017) 110–126.
[29] A.J. Martín, G.O. Larrazábal, J. Pérez-Ramírez, Green Chem. 17 (2015) 5114–5130.
[30] Y. Jiang, A.V. Virkar, J. Electrochem. Soc. 150 (2003) A942.
[31] O. Costa-Nunes, R.J. Gorte, J.M. Vohs, J. Power Sour. 141 (2005) 241–249.
[32] P. Kim-Lohsoontorn, Y.-M. Kim, N. Laosiripojana, J. Bae, Int. J. Hydrogen Energy 36 (2011) 9420–9427.
[33] R. Nishida, P. Puengjinda, H. Nishino, K. Kakinuma, M.E. Brito, M. Watanabe, H. Uchida, Rsc Adv 4 (2014) 16260–16266.
[34] Y. Luo, W. Li, Y. Shi, Y. Wang, N. Cai, Int. J. Hydrogen Energy 42 (2017) 25130–25142.